The K_L/μ Detector Subsystem for the BELLE Experiment at the KEK B-factory

A. Abashian [h], K. Abe [b], K. Abe [f], S. Azuchi [f], P.K. Behera [g], S. Chidzik [d], S. Chinomi [c], K. Gotow [h], F. Haitani [e], H. Hanada [f], K. Hanagaki [d], Y. Hoshi [e], Y. Igarashi [f], Y. Inoue [c], N. Kawamura [a], K. Korotushenko [d], D. Marlow [d], N. Morgan [h], T. Nagamine [f], M. Nakajima [f], T. Nakajima [f], E. Nakano [c], S. Narita [f], K. Neichi [e], L. Piilonen [h], E. Prebys [d], H. Sakai [c], W. Sands [d], S. Schrenk [h], T. Takahashi [c], T. Takayama [f], Y. Teramoto [c], M. Ueki [f], M. Yamaga [f], A. Yamaguchi [f],and H. Yuta [a]

[a] *Aomori University, Aomori 030-0943, Japan*

[b] *High Energy Accelerator Research Organization (KEK), Tskukuba, Ibaraki 305-0801, Japan*

[c] *Osaka City University, Osaka 558-8585, Japan*

[d] *Princeton University, Princeton, NJ 08544, USA*

[e] *Tohoku-Gakuin University, Tagajo 985-8537, Japan*

[f] *Tohoku University, Sendai 980-8578, Japan*

[g] *Utkal University, Vani Vahar, Bhubaneswer-751 004, India*

[h] *Virginia Polytechnic Institute and State University, Blacksburg, VA 24061-0435, USA*

29 September 1999

Abstract

The K_L and muon detection subsystem (KLM) of the BELLE experiment at the KEK-B asymmetric B-factory is described. The system consists of glass-electrode resistive plate counters installed within the segmented flux return iron of the BELLE superconducting solenoid. The design and construction of the detectors, including the gas distribution system and readout electronics, are described in detail. The operating characteristics and performance with cosmic rays and e^+e^- collision data are presented.

Preprint submitted to Elsevier Preprint *29 September 1999*

1 Introduction

The BELLE detector is designed to measure the properties of the particles produced in the collisions of electrons and positrons at the KEK-B asymmetric B-factory at the High Energy Accelerator Research Organization[1]. The primary physics goal of this experiment is the measurement of charge conjugation and parity (CP) nonconservation via certain exclusive decays of heavy mesons containing b quarks[2]. Many of these decay modes require the identification of muons from the semileptonic decay of B and D mesons and from $J/\psi \rightarrow \mu^+\mu^-$. In the Standard Model, CP nonconservation is incorporated in an imaginary phase in the 3x3 quark sector mixing matrix known as the CKM matrix[3]. This phase can be probed, for example, in the decay $B^0 \rightarrow J/\psi \mathrm{K_L}$, which provides a measurement of the phase angle ϕ_1 in one of the triangles that can be formed from the unitarity constraint on the CKM matrix. With this physics goal in mind the KLM subsystem was designed to identify $\mathrm{K_L}$'s and muons with high efficiency over a broad momentum range greater than 600 MeV/c. The barrel-shaped region around the interaction point covers an angular range from 45° to 125° in polar angle and the endcaps in the forward and backward directions extend this range to 20° and 155°.

The KLM system consists of alternating layers of charged particle detectors and 4.7 cm thick iron plates. There are 15 detector layers and 14 iron layers in the octagonal barrel region and 14 detector layers and 14 iron layers in each of the forward and backward endcaps. The iron plates provide a total of 3.9 interaction lengths of material for a particle travelling normal to the detector planes. In addition, the electromagnetic calorimeter (CsI) provides another 0.8 interaction lengths of material to convert $\mathrm{K_L}$'s. Figure 1 shows the BELLE detector with the segmented magnetic flux return iron in the barrel and endcap regions. The $\mathrm{K_L}$ particles that interact in the iron or CsI produce a shower of ionizing particles. The location of this shower determines the $\mathrm{K_L}$'s direction; but fluctuations in the size of the shower do not allow a useful measurement of the $\mathrm{K_L}$ energy. The multiple layers of charged particle detectors and iron allow discrimination between muons and charged hadrons ($\pi^\pm$ or $\mathrm{K}^\pm$) based upon their range and transverse scattering. The muons travel significantly farther with smaller deflections on average than the strongly interacting hadrons.

The charged particle detection is provided by glass-electrode resistive plate counters (RPCs)[4–8]. Glass RPCs have a long history dating back to the early 1970's [9], but this is the first experiment in which large area glass detectors

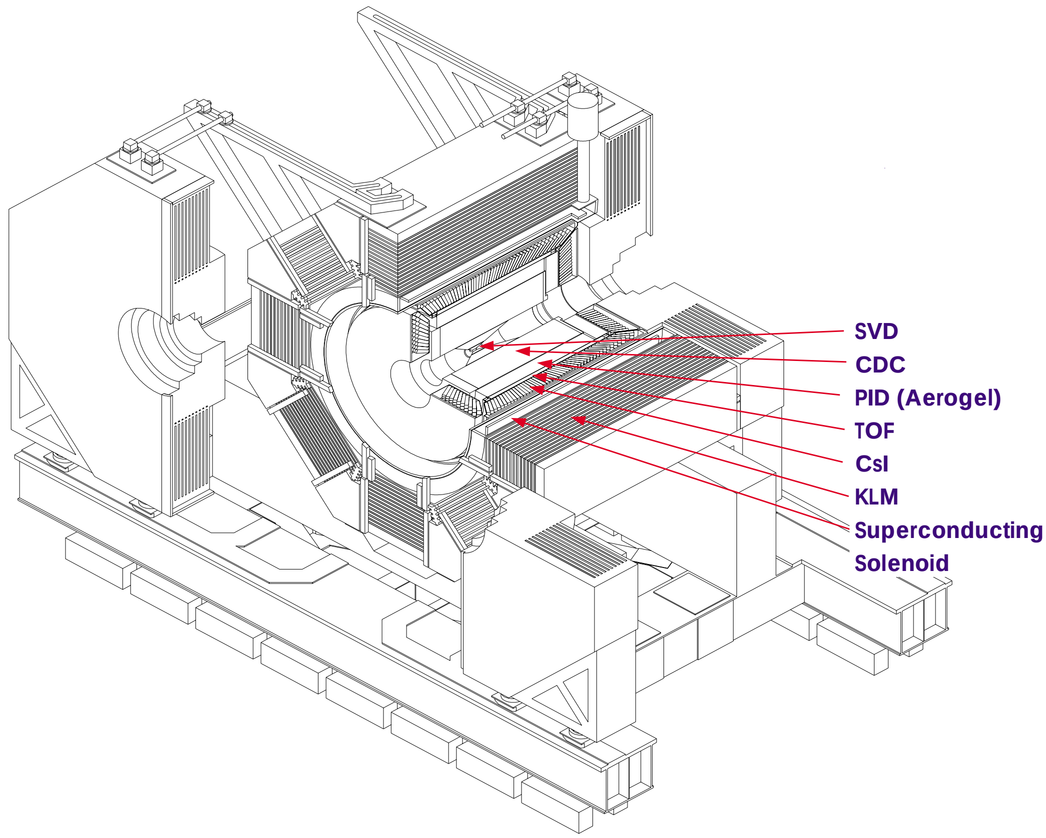

Fig. 1. *The BELLE detector.*

operated at atmospheric pressure have been used. Resistive plate counters have two parallel plate electrodes with high bulk resistivity ($> 10^{10}\ \Omega\,\mathrm{cm}$) separated by a gas-filled gap. In streamer mode, an ionizing particle traversing the gap initiates a streamer in the gas that results in a local discharge of the plates. This discharge is limited by the high resistivity of the plates and the quenching characteristics of the gas. The discharge induces a signal on external pickup strips, which can be used to record the location and the time of the ionization.

The details of the RPC module design and construction and operating characteristics are described in section 2. The gas mixing and distribution system with pressure control, which is vital to the successful stable operation of these glass detectors, is described in section 3. In section 4 we describe the readout electronics. Finally, the performance of the KLM subsystem for detecting K_L's and muons is presented in section 5.

2 Glass Resistive Plate Counters

2.1 Barrel Modules

There are minor differences between the barrel modules, which were built in the United States, and the endcap modules which were built in Japan. The barrel resistive plate counters consist of two parallel sheets of 2.4 mm thick commercially available float glass (73% silicon dioxide, 14% sodium oxide, 9% calcium oxide, and 4% trace elements). The bulk resistivity of the glass is $10^{12} - 10^{13}$ Ω cm at room temperature. The plates are separated by 1.9 mm thick extruded noryl spacers epoxied to both plates using 3M 2216 epoxy. Figure 2 shows a barrel RPC with the spacers placed every 10 cm in such a way that they channel the gas flow through the RPC to provide uniform gas composition throughout the active volume. A T-shaped noryl spacer was epoxied around the perimeter forming a gas tight unit. The spacers have cross sections shown in Figure 3. They were designed with concave regions for the epoxy joints and were extruded to an accuracy of ± 0.05 mm. Tilting table tops were used to lift the RPCs into a vertical orientation to avoid flexing the epoxy joints. After assembly, the RPCs were always moved in a vertical orientation or supported by a rigid flat surface. The barrel RPCs are rectangular in shape and vary in size from 2.2×1.5 m^2 to 2.2×2.7 m^2.

To distribute the high voltage on the glass, the outer surface was coated with Koh-i-noor 3080F india ink. The ink was mixed 30% black and 70% white by weight to achieve a surface resistivity of $10^6 - 10^7 \Omega/\square$. This resistivity is chosen so that this surface does not shield the discharge signal from the external pickup pads but is small compared to the resistivity of the glass to provide a uniform potential across the entire surface.

The cross section of a superlayer in Figure 4 shows the two RPCs sandwiched between orthogonal pickup strips with ground planes for signal reference and proper impedance. This two-RPC and two-readout-plane sandwich is enclosed

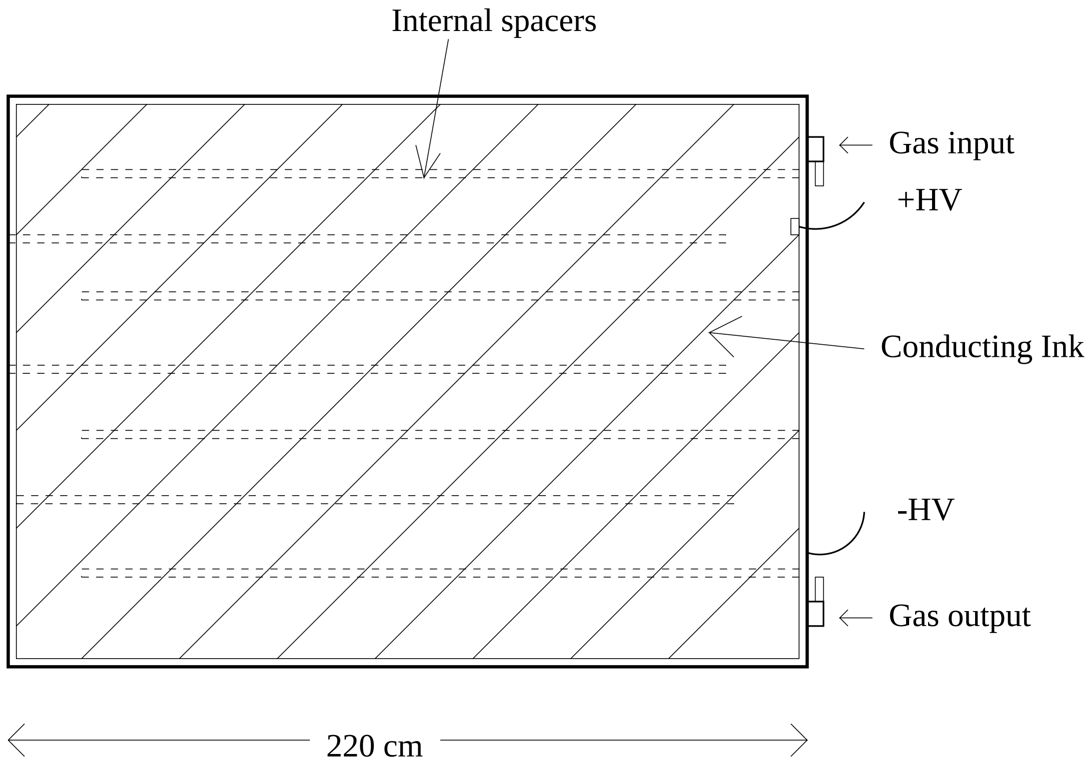

Fig. 2. *Barrel RPC showing internal spacers.*

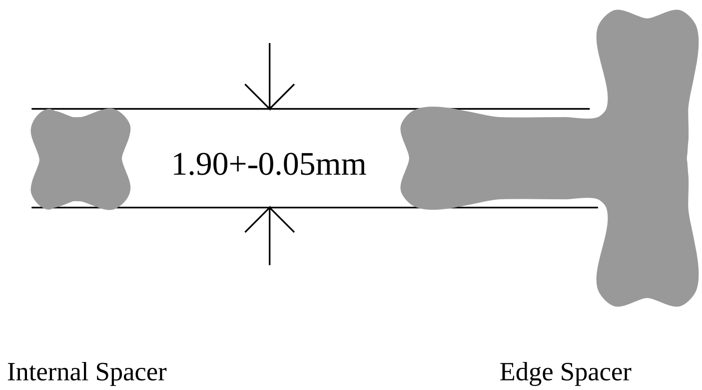

Fig. 3. *Internal spacer and edge spacer cross sections.*

in an aluminum box and is less than 3.7 cm thick. Each RPC is electrically insulated with a double layer of 0.125 mm thick mylar. Signals from both RPCs are picked up by copper strips above and below the pair of RPCs, providing a three-dimensional space point for particle tracking. Multiple scattering of particles as they travel through the iron is typically a few centimeters. This sets the scale for the desired spatial resolution of the KLM system. The pickup strips in the barrel vary in width from layer to layer but are approximately 50 mm wide with lengths from 1.5 to 2.7 m. The geometry of the pickup strips was chosen so that the pickup strip behaves as a transmission line with a characteristic impedance of $\sim 50\Omega$ to minimize signal reflections at the junction with the twisted-pair readout cable. The barrel modules have a 100 Ω resistor connecting the pickup strip to ground at the cable end of the pickup strip to create an effective 50 Ω impedance at that point. This reduces the size of the signal which reaches the readout boards for the barrel modules by a factor of two.

The double-gap design provides redundancy and results in high ($\geq 98\%$) superlayer efficiency, despite the relatively low (90% to 95%) single-layer RPC efficiency. In particular, the effects of dead regions near the spacers are minimized by offsetting their locations for the two RPCs that comprise a superlayer. To provide overall operational redundancy, care is taken to supply gas and HV independently for each RPC layer so that the superlayer can continue to operate even if a problem develops with one RPC.

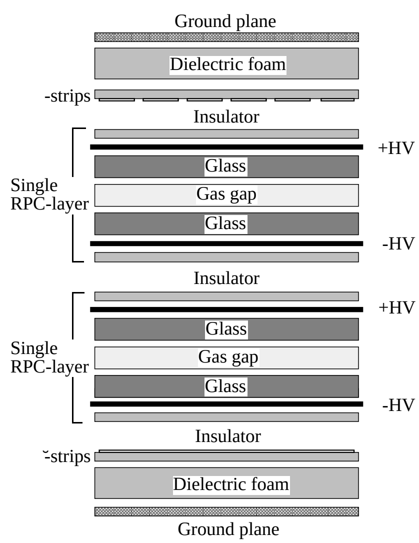

Fig. 4. *Cross section of a superlayer module.*

Each barrel module has two rectangular RPCs with 48 z pickup strips perpendicular to the beam direction. The smaller 7 superlayers closest to the interaction point have 36 ϕ strips and the outer 8 superlayers have 48 ϕ strips orthogonal to the z strips. The backward region of the upper octant has modules that are 63 cm shorter than the modules in the other octants in order to accommodate plumbing for the cooling of the superconducting solenoid. This chimney region can be seen in Figure 1. This amounts to less than 2% of the solid angle of the barrel coverage and has a minimal effect on the acceptance since it is in the backward hemisphere.

Approximately 18 superlayers weighing an average of 110 kg each were crated with 8 cm of rigid foam packing material surrounding them. They travelled by land and sea from the United States to Japan. The glass RPCs are relatively robust except for overpressure situations which can push the two sheets of glass apart, breaking the glass-spacer epoxy joint. To avoid this hazard, the gas volume was not sealed during shipping. Relief bubblers protect the RPCs during operation. The RPCs were checked for gas leaks prior to installation. The sensitivity of our measurement was about 0.05 cc/min and this was the leak rate limit we set for all installed RPCs.

2.2 Endcap Modules

The glass used in the endcap RPCs is 2.0 mm thick and has a chemical content of SiO_2 70-74%, CaO 6-12%, Na_2O 12-16%, Al_2O_3 0-2%, and MgO 0-4%. The epoxy used to attach the spacers and seal the gas volume was 3M DP460. The high voltage distribution on the glass was accomplished by applying a conducting carbon tape SHINTRON STR-9140 with a surface resistivity of $10^7 - 10^8 \Omega/\Box$ to the outer surface of the glass.

Each superlayer module contains 10 pie-shaped RPCs as shown in Figure 5. The θ strips are 36 mm wide and vary in length from 2 to 5 m. The ϕ strips are 1.83 m long and vary in width from 19 mm to 47 mm. Figure 6 shows an endcap superlayer module cutaway view with the 96 ϕ and 48 θ pickup strips in each module.

2.3 Efficiency and Resolution

In this section we describe the general characteristics of the glass-electrode RPCs[13]. The relatively high resistance of the glass, $\sim 5 \times 10^{12}\ \Omega$ cm, limits

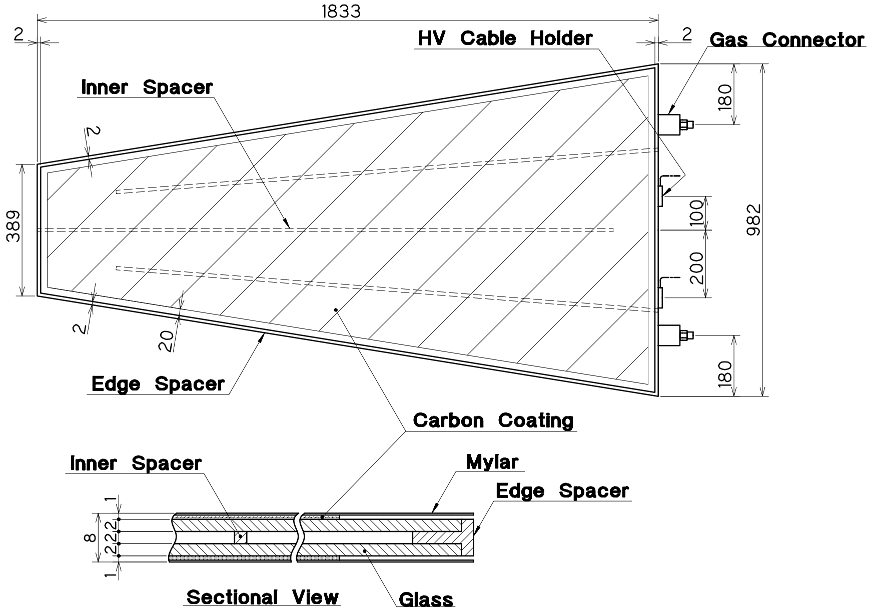

Fig. 5. *Endcap RPC showing internal spacers.*

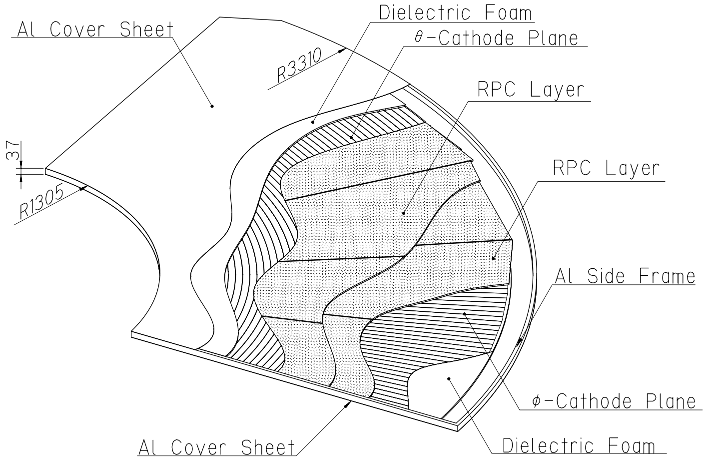

Fig. 6. *Cut-away view of an endcap superlayer module.*

the rate capability of these counters to ~ 0.2 Hz/cm^2, but in this application where the particle flux is little more than the cosmic ray flux, the detectors function with high efficiency. The signals typically have a 100 mV peak into a 50 Ω termination and have a full width at half maximum of less than 50 ns. A typical RPC has a singles rate of less than 0.03 Hz/cm^2 with few spurious discharges or afterpulses. We operate the barrel modules at 4.3 kV/mm with a signal threshold of 40 mV and the endcap modules at 4.2 kV/mm with a signal threshold of 70 mV. The choice of different operating points is due to the differences in the characteristics of the pickup strips for the barrel and the endcap.

Figure 7 shows the efficiency versus voltage for each of the RPC planes in an endcap superlayer. These data were obtained using cosmic rays that penetrate the endcap. The efficiency is obtained by triggering on and tracking a particle using the other superlayers, calculating the expected location of the track as it passed through this superlayer, and looking to see if a hit was recorded at that location (± 1 strip). The efficiency is then the ratio of the number of hits found to the number expected. In Figure 8 an efficiency map with a grid determined by the readout strips is shown. With only one RPC layer active, the RPC edges are clearly seen. The area near the internal spacers, which are 2 mm wide, is inactive. Care was taken to insure that the internal spacers in the two layers do not overlap. With both planes active, which is the normal operating condition, the superlayer acts as a logical "OR" for hits in either RPC layer and has an average efficiency that is typically over 98%.

Cosmic rays were used to map the efficiency and to determine the relative positions of all of the superlayer modules. Additionally, the response of the modules to penetrating muons was measured and the results were used as input to the simulation programs. For example, for a given operating voltage and discriminator threshold, a penetrating muon generates hits on an average of 1.4 strips per layer in the barrel modules and 1.9 strips per layer in the endcap modules.

The spatial resolution of the modules is shown in Figure 9. This residual distribution is the difference between the measured and predicted hit location using a track that has been fitted using hits in the adjacent layers. The multiplicity referred to is the number of strips in the superlayer that have signals over threshold. When two or more adjacent strips have signals over threshold, the hit location used for particle tracking is calculated by averaging the strips together. With one or two strips hit the standard deviation is 1.1 cm. With three strips it increases to 1.7 cm and with four strips it is 2.9 cm. The multiplicity weighted standard deviation is for this residual distribution is 1.2 cm and gives angular resolution from the interaction point of better than 10 mrad. The TDCs provide time information for the hits that can be used to eliminate hits which are out of time with respect to the e^+e^- collision. The time resolution of the KLM system is a few ns.

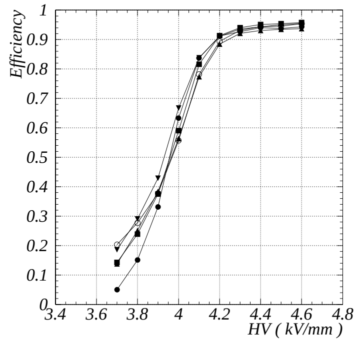

Fig.7-a. Efficiency plateau for 5 typical top-layer RPCs.

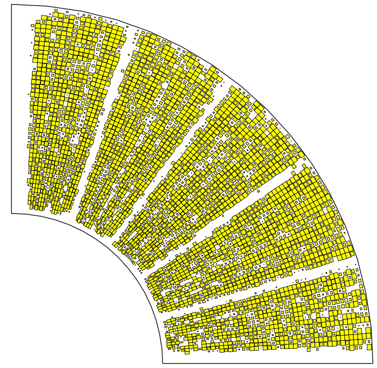

Fig.8-a. Efficiency map of top-layer RPCs in endcap quadrant.

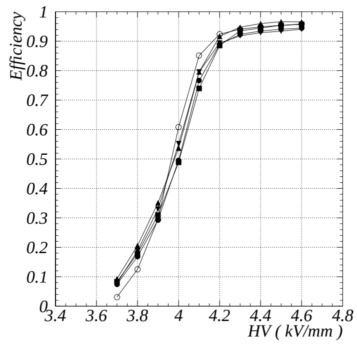

Fig.7-b. Efficiency plateau for 5 typical bottom-layer RPCs.

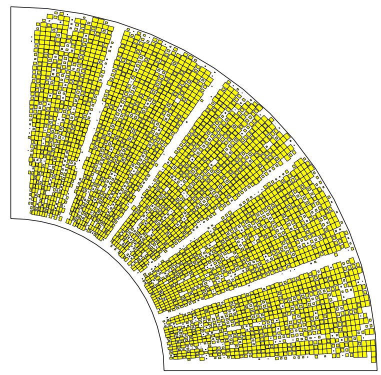

Fig.8-b. Efficiency map of bottom-layer RPCs in endcap quadrant.

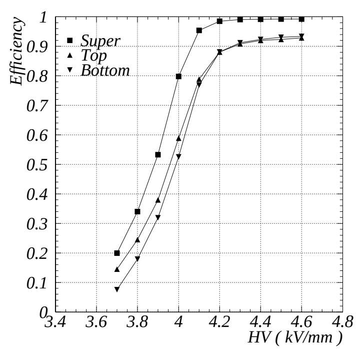

Fig.7-c. Efficiency plateau for RPCs alone and in combination in a typical superlayer.

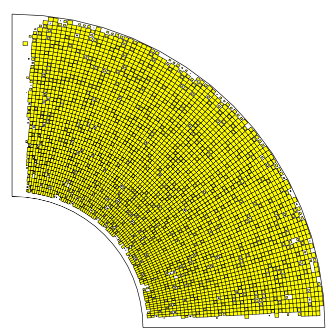

Fig.8-c. Efficiency map of superlayer in endcap quadrant.

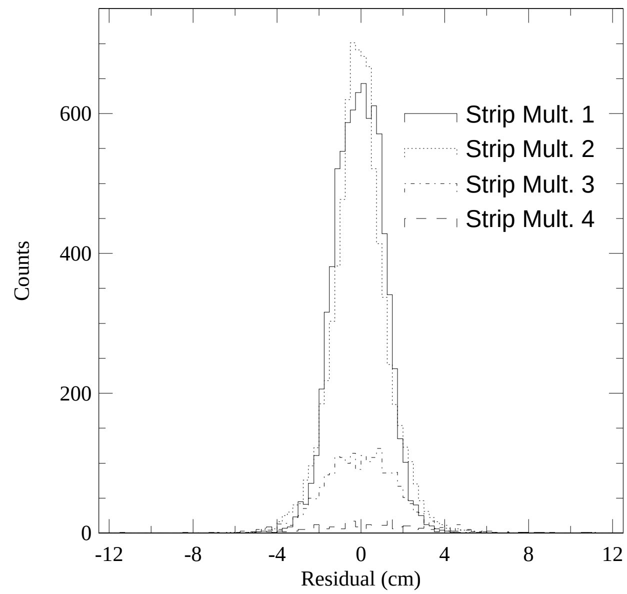

Fig. 9. Spatial resolution of a superlayer.

3 K_L and Muon Subsystem

3.1 High Voltage System

During data taking, the modules typically operate with a total gap voltage of 8 kV. Rather than grounding one electrode and using a single-ended supply to bias the other, we chose to separately apply positive voltage to the anodes and negative voltage to the cathodes. This approach minimizes the potential to ground on connectors, cables, and surfaces as a precaution against external discharges through and around insulators. Moreover, it helps reduce the overall HV system cost since modules capable of producing voltages in excess of 7.5 kV are less common and therefore more costly.

We are using the LeCroy VISyN high voltage system, which consists of Model

Table 1

Gas	Symbol	mol.weight	density
argon	Ar	39.95	1.784 g/l (0 deg C, 1 atm)
butane-silver	C_4H_{10}	58.12	2.6 g/l (0 deg C, 1 atm)
HFC-134a	CH_2FCF_3	102.0	4.5 g/l

1458 mainframes and plug-in modules (the Model 1468P for the anodes and the Model 1469N for the cathodes). The cathodes are set at -3.5 kV; the anodes are set at +4.7 kV for the barrel RPCs and +4.5 kV for the endcap RPCs. To reduce the system cost, the anode planes are ganged together and controlled by one positive high voltage channel. In the barrel, eight anode planes are ganged together; in the endcaps, five anode planes are ganged together. The total current drawn by the RPCs during operation is approximately 5 mA or $\sim 1\ \mu\text{A/m}^2$ of RPC area. For properly operating chambers, most of this current flows through the noryl spacers.

3.2 Gas Mixing and Distribution

We have investigated gas mixtures in search of an environmentally friendly and non-combustible mixture that provides high detection efficiency and stable RPC operation[16]. We compared 16 different mixtures with butane concentrations of 4, 8, 12, and 25% and argon concentrations of 20, 25, 30, and 35% with the balance of the gas being HFC-134a. The RPC performance in terms of efficiency, dark current, singles rate, and timing resolution was compared at an operating point 200 V/mm above the knee of the efficiency plateau curve. The butane reduces the presence of afterpulses by absorbing photons from the initial discharge. The nonflammable limit for the butane is about 12% at the mixing ratio of 1:1 argon:HFC-134a. We found very little difference between the flammable and nonflammable mixtures and have chosen a non-combustible mixture of 62% HFC-134a, 30% argon, and 8% butane-silver. Table 3.2 lists some basic physical parameters of these gases. Butane-silver is a mixture of approximately 70% n-butane and 30% iso-butane. The cost of butane-silver is one tenth of the cost of 99.5% pure iso-butane.

There are two separate banks of bottles for each type of gas. When one side becomes empty, the supply line automatically switches to the other. Tank

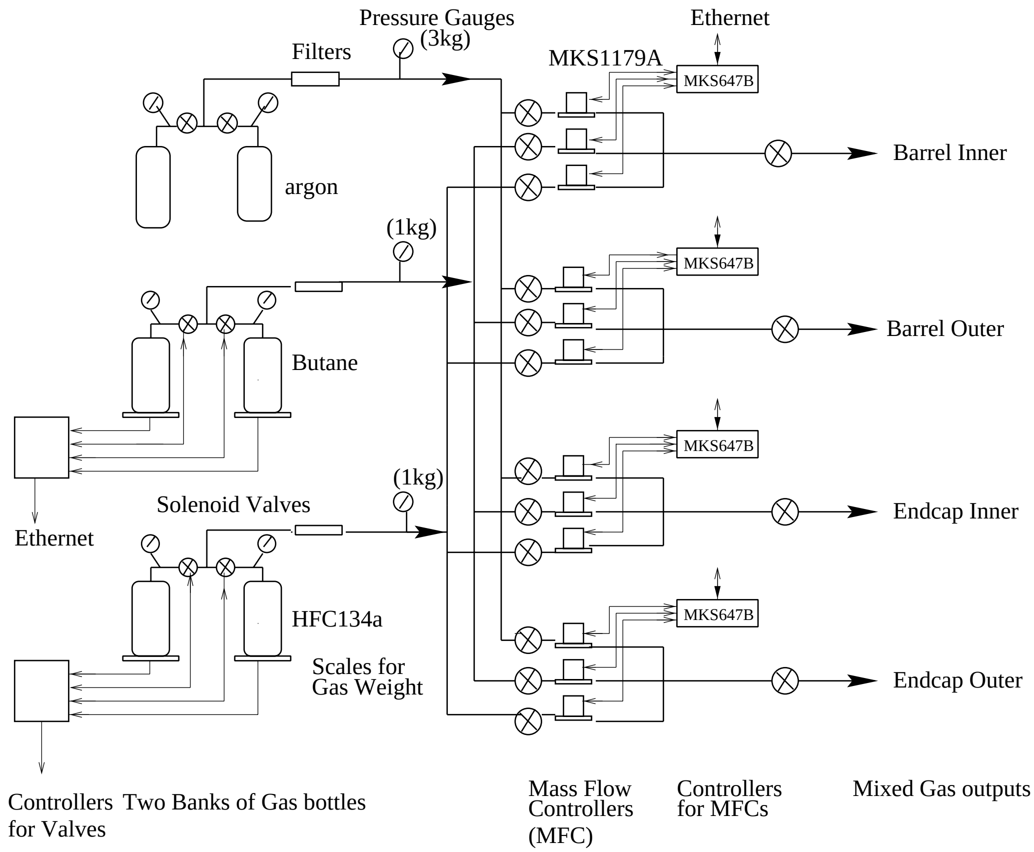

Fig. 10. The gas mixing system.

quantities are measured by weight for butane and HFC-134a and by pressure for argon. A diagram of the mixing system is shown in Figure 10. The three gases are sent to MKS model 1179A mass flow controllers for mixing in the appropriate ratios. There are four gas mixing systems - one for the inner RPCs in the barrel superlayers, one for the barrel outer RPCs, one for endcap inner RPCs, and one for endcap outer RPCs. The flow rates from the mass flow controllers are monitored via a network connection and the high voltage is automatically lowered if a deviation from the desired flow rate is detected. During normal operation, we flow a total of 4.5 ℓ/min, which corresponds to approximately one volume change per day.

A diagram of the KLM gas distribution system is given in Figure 11. The gas distribution system is designed to provide an independent gas supply to each RPC in a superlayer so that if one supply line fails for any reason the other RPC in the superlayer will still be operational. Mixed gas is distributed to 704 individual RPC layers through a series of manifolds. To insure uniform distribution of the flow without the need for tedious adjustments, a “flow resistor” was inserted in series upstream of each RPC. These devices are 10-cm-long stainless-steel tubes with an inner diameter of 254 μm. The flow impedance of the tubes is about ten times larger than that of an RPC layer. The flow rate from the manifolds is then determined by the flow resistor (uniform to about 15%) and largely independent of variations in the flow resistance of individual RPCs.

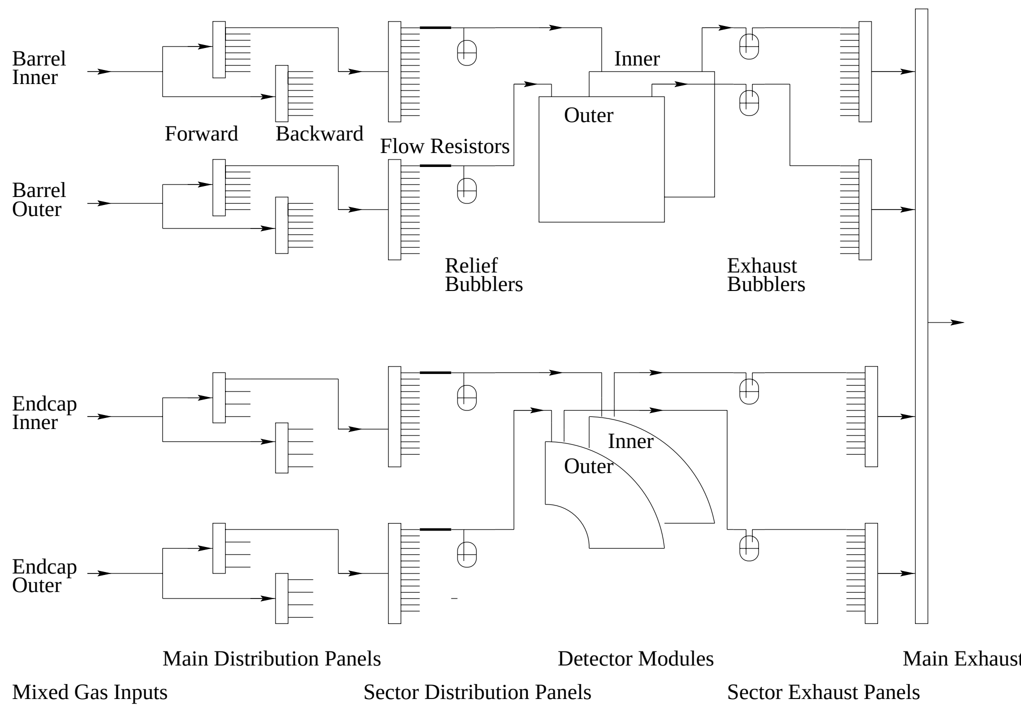

Fig. 11. The gas distribution system.

The exhaust system is shown in Figure 12. Tests showed that the epoxy joints between the glass plates and the internal spacers begin to detach when a barrel RPC is pressurized above 50 mmAq. When this happens, the RPC is still gas tight, but detector performance begins to deteriorate because the gap in the mid-region becomes larger than the nominal value. When more than 150 mmAq pressure is applied, the epoxy joints between the glass plates and the edge-spacer begin to fail and a gas leak develops. Active control of the exhaust pressure and relief bubblers at various points in the system were introduced to avoid these overpressure situations.

For reasons of safety, the gas is not exhausted into the experimental hall. The exhaust gas from each channel goes through a bubbler to a common manifold,

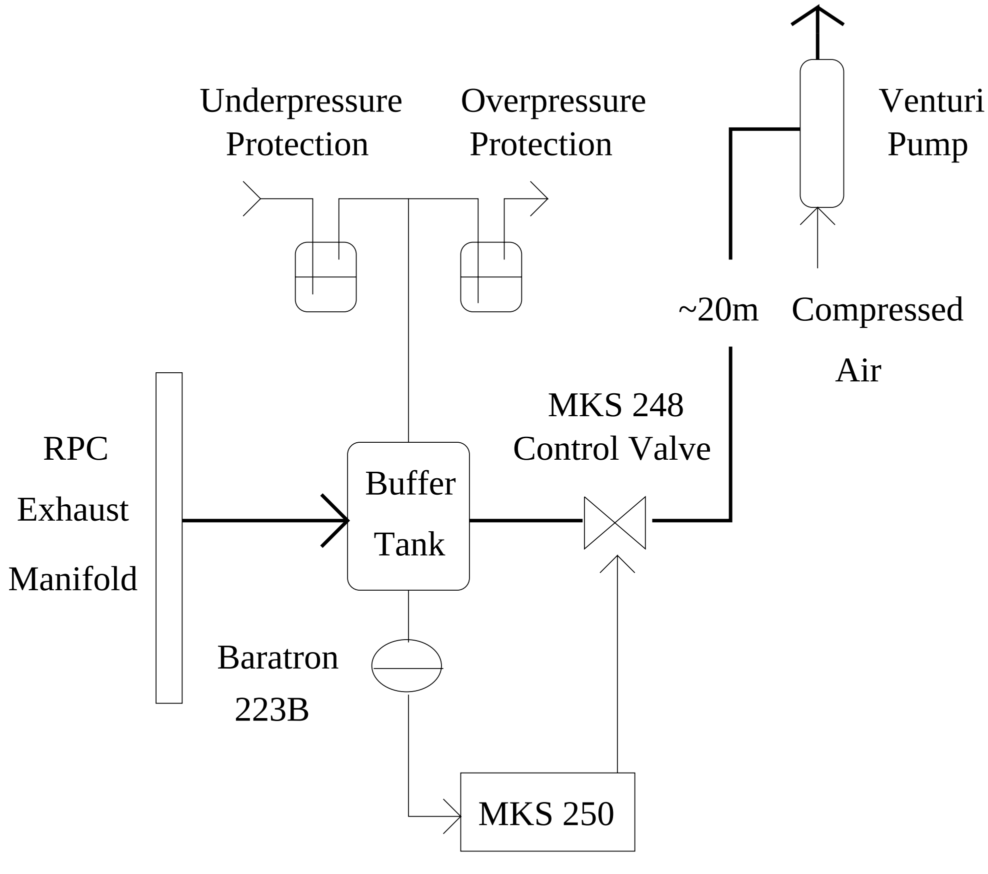

Fig. 12. The gas exhaust and pressure control system.

and then is taken out of the experimental hall through a 20 m vertical exhaust line. Since the average density of the mixed gas is significantly larger than that of air (3.53 g/ℓ compared with 1.3 g/ℓ for air), the gas volume that fills the exhaust line corresponds to about 40 mmAq pressure at the level of the RPCs. We reduce this pressure differential to nearly zero by using a venturi pump and pressure-regulated buffer volumes in the exhaust lines. The venturi pump provides a constant suction that is somewhat larger than what is needed to pump the gas to the surface. A feedback loop consisting of a differential pressure transducer (Baratron #223B), an electronic control unit (MKS #250), and a variable-impedance proportional solenoid valve (MKS Model #248) adjusts the exhaust impedance to maintain the exhaust buffers at the desired value.

4 Readout Electronics

Readout of 38k pickup strips is accomplished with the use of custom-made VME based discriminator/time-multiplexing boards developed by Princeton University and Osaka City University. The system consists of the signal discrimination and multiplexing boards, crate controller boards (one per crate) for crate-wide control and data processing, string controller boards for downloading and controlling multiple readout crates, and Fastbus time-to-digital converters.

The discriminator boards are 6U size VME boards with 96 input channels per board. A comparator (MAX908CPD) is used to generate a logic signal if the voltage on the input channel exceeds the threshold voltage. This threshold can be selected via a programmable digital-to-analog converter to be any value from -250 mV to +250 mV. A time multiplexor scheme combines hit information from 12 RPC channels into a single high-speed serial data stream that is passed to a LeCroy 1877 pipelined time-to-digital converter (TDC). The multiplexing is accomplished with the use of a Xilinx XC4005E field programmable gate array (FPGA). A schematic diagram of the readout electronics is shown in Figure 13. In addition, the logical OR of the hits for each 12-channel group is generated and is available for use as a fast trigger signal.

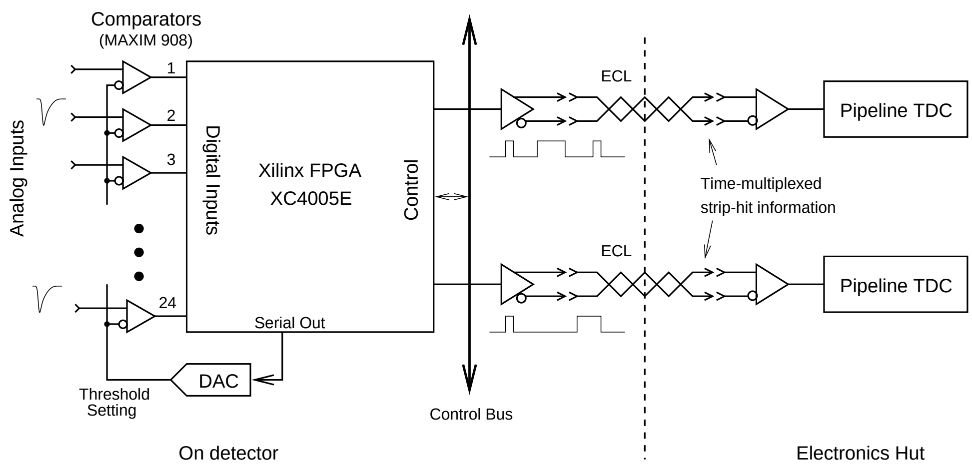

Fig. 13. Schematic of the RPC readout electronics.

Each VME crate has a crate controller board which transmits control data from the string controller to the discriminator boards via the dedicated VME backplane. A 10 MHz clock signal from the crate controller board is distributed throughout the crate for use by the discriminator boards in time sequencing the RPC hits. The string controller is a multifunction VME-compatible board using a Xilinx 4013 programmable gate array to allow downloading and control of a string of up to 8 RPC readout crates. Once the discriminator board is programmed, the time sequenced hit information travels directly from each 96 channel board to 8 TDC channels residing in a Fastbus crate. In this manner, 38k RPC channels are reduced to 3200 Fastbus TDC channels, resulting in a significant cost savings. It is also possible to read RPC strip-hit data directly through the string controllers, as was done during system commissioning when the production TDC system was not yet available.

5 Performance

5.1 Operating Experience

The system has been operating for approximately one year. When we first installed the modules, we used 1/4 inch diameter flexible polyolefin tubing from the gas distribution manifolds to the RPCs. After several weeks of operation, we noticed an increase in the dark current drawn by some of the RPCs and a corresponding decrease in efficiency. This was found to be due to water vapor in the air migrating through the tubing and entering the RPC active volume. Some of these tubes were as long as 12 meters and we measured concentrations of H_2O as high as 2000 parts per million in some RPC exhaust lines. Approximately 50% of the barrel modules were affected. The efficiency of some barrel RPCs dropped below 50% before corrective measures were taken. We replaced the plastic tubing with copper tubing to prevent additional water vapor entering the RPCs. The contaminated RPCs eventually dried out and have recovered most of their lost efficiency. Other than the initial water vapor problem, which has been solved, the RPCs have operated reliably and with an average efficiency of better than 97%.

5.2 $\mathrm{K_L}$ *detection*

In this section we present results obtained with e^+e^- collider data taken during the summer 1999 commissioning run of the KEK B-factory. The identification of K_L particles involves first associating KLM hits into clusters. Charged particles are measured in the inner tracking chambers and extrapolated into the KLM detectors. Clusters within 15 degrees of an extrapolated charged particle are excluded as K_L cluster candidates. For isolated clusters, the center of gravity of the hits is calculated and used to determine the direction of the cluster from the interaction point. In Figure 14, we show a histogram of the difference between the K_L cluster candidate direction and the missing momentum vector direction. The missing momentum vector is calculated using all of the other measured particles in the event.

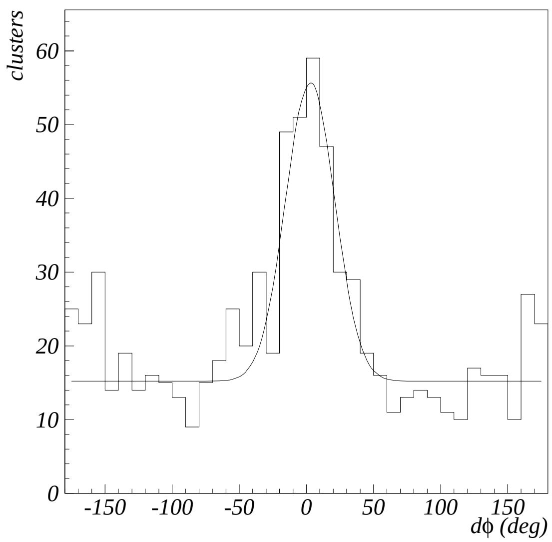

Fig. 14. Difference between the neutral cluster direction and the missing momentum direction.

This histogram shows a clear peak where the neutral cluster measured in the KLM is consistent with the missing momentum in the event. Large deviation of the missing momentum direction from the neutral cluster direction is mainly due to undetected neutrinos and particles escaping the detector acceptance. The number of neutral clusters per event is compared in Figure 15 to a Monte Carlo simulation of the predicted number of K_L clusters per event. The average number of K_L clusters per event is 0.5. The agreement with the prediction gives us confidence that the detector and our reconstruction software are performing correctly.

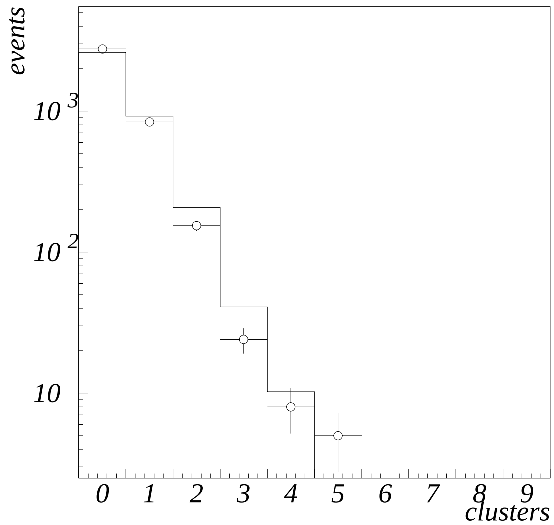

Fig. 15. Number of neutral clusters per event.

5.3 Muon detection

We have used cosmic rays, which are primarily muons, as a calibration tool to measure the superlayer efficiency and resolution. With the BELLE solenoid and central drift chamber measuring the cosmic ray momentum, we can plot the detection efficiency as a function of particle momentum. Below 500 MeV/c, the muon does not reach the KLM detectors. A comparison of the measured range of the particle to the predicted range for a muon of the measured momentum, in conjunction with the amount of scatter of the particle as it passes through the multiple layers of iron, allows us to assign a likelihood to its being a muon. In Figure 16 the muon detection efficiency versus momentum is shown for a likelihood cut of 0.66. Some fraction of charged pions and kaons will be misidentified as muons. In the e^+e^- collision data, we have a sample of $\mathrm{K_S} \to \pi^+\pi^-$ which we have used to measure this fake rate. The fraction of pions which are misidentified as muons is shown in Figure 17, again with a muon likelihood cut of 0.66. The histogram is a Monte Carlo simulation to be compared with the measurement. Above 1.5 GeV/c we have a muon identification efficiency of better than 90% with a fake rate of less than 5%.

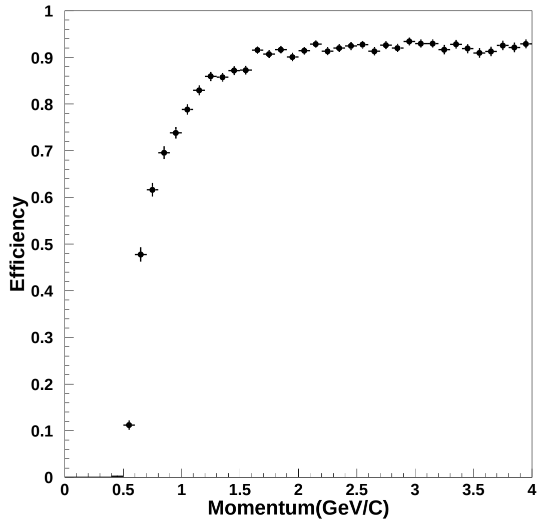

Fig. 16 Muon detection efficiency versus momentum.

6 Summary

We have built and operated a 2200 m^2 K_L and muon particle detector for the BELLE experiment at the KEK B-factory using glass-electrode resistive plate counters. Three gases are mixed and distributed to 704 RPC layers with pressure control to prevent overpressurization of the detectors. A discriminator/time multiplexing VME based readout system using field-programmable gate arrays reduces the number of time-to-digital converters by a factor of 12, significantly reducing the instrumentation costs. The detectors have $\sim$ 98% detection efficiency for minimum ionizing particles. The detection of K_L's and muons is consistent with expectations based on Monte Carlo simulations, and the system should provide valuable information used for the measurement of CP violation parameters as well as many other physics processes.

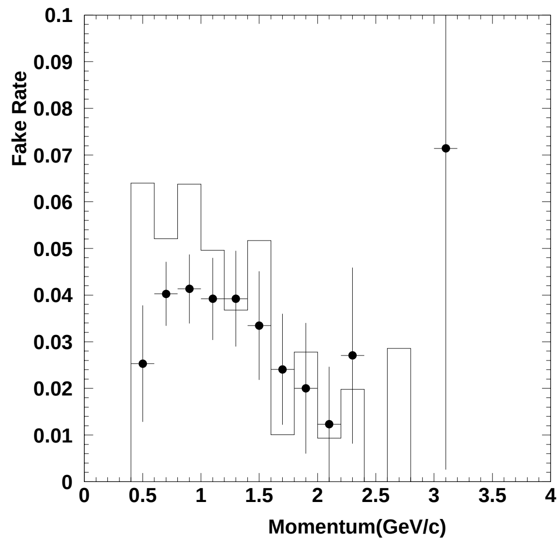

Fig. 17. Fake rate versus momentum.

7 Acknowledgements

This work was supported by the U.S.-Japan Cooperative Research Program in High Energy Physics, the Japanese Ministry of Education, Science, Culture, and Sports (Monbusho), and the U.S. Department of Energy.

References

[1] B Physics Task Force, Progress Report on Physics and Detector at KEK Asymmetric B Factory, KEK Report 92-3, May 1992.

[2] BELLE Collaboration, A Study of CP Violation in B Meson Decays - Technical Design Report, KEK Report 95-1, April 1995.

[3] M. Kobayashi and T. Maskawa, Prog. Theo. Phys., **49**, 652 (1973), N.Cabbibo, Phys. Rev. Lett. **10**, 531 (1963), L. Wolfenstein, Phys. Rev. Lett. **51**, 1945 (1983).

[4] R. Cardarelli *et al*, Nuclear Instruments and Methods **A263** (1988) 20.

[5] Yu. N. Pestov, Nuclear Instruments and Methods **196** (1982) 45.

[6] R. Santonico and R. Cardarelli, Nuclear Instruments and Methods **187** (1981) 377.

[7] F. Romano *et al*, Conference Proceedings of the Vulcano Workshop, Vulcano, Italy (1990) 337.

[8] E.Gorini, Nucl. Phys. **23B** (1991) 249. L. Antoniazzi, *el al*, Nuclear Instruments and Methods **A307** (1991) 312.

[9] V. V. Parkhomchuck *et al*, Nuclear Instruments and Methods **93** (1971) 269, W. B. Atwood *et al*, Nuclear Instruments and Methods **206** (1983) 99.

[10] C. R. Wuest, R. M. Bionta, and I. R. Pless, "Resistive Plate Chambers for the GEM Detector Muon Trigger System," GEM Collaboration, January 18, 1993.

[11] M. Bertino *et al*, Nuclear Instruments and Methods **A283** (1989) 654.

[12] M. Iori and F. Massa, Nuclear Instruments and Methods **A306** (1991) 159.

[13] N. Morgan, Second International Workshop on Resistive Plate Chambers and Related Detectors, Pavia, Italy, (1995) 101.

[14] G. Battistoni *et al*, Nuclear Instruments and Methods **A270** (1988) 190.

[15] G. Battistoni *et al*, Nuclear Instruments and Methods **202** (1982) 459.

[16] A. Yamaguchi, Fourth International Workshop on Resistive Plate Chambers and Related Detectors, Naples, Italy, (1997) 281.

8 Figure Captions

Figure 1. The BELLE Detector.

Figure 2. Barrel RPC showing internal spacers.

Figure 3. Internal spacer and edge spacer cross sections.

Figure 4. Cross section of a superlayer module.

Figure 5. The endcap RPC showing internal spacers.

Figure 6. Cut-away view of an endcap superlayer module.

Figure 7. The efficiency versus voltage.

Figure 8. The efficiency map of an endcap superlayer.

Figure 9. Spatial resolution of a superlayer.

Figure 10. The gas mixing system.

Figure 11. The gas distribution system.

Figure 12. The gas exhaust and pressure control system.

Figure 13. Schematic of the RPC readout electronics.

Figure 14. Difference between the neutral cluster direction and the missing momentum direction.

Figure 15. Number of neutral clusters per event.

Figure 16. Muon detection efficiency versus momentum.

Figure 17. Fake rate versus momentum.